New regime of homogeneous flow in the deformation map of metallic glasses: elevated temperature nanoindentation experiments and mechanistic modeling

Christopher A. Schuh [a,*], Alan C. Lund [a], T.G. Nieh [b]

[a] *Department of Materials Science and Engineering, Massachusetts Institute of Technology, 77 Massachusetts Avenue, Room 8-211, Cambridge, MA 02139, USA*
[b] *Department of Materials Science and Engineering, University of Tennessee, Knoxville, TN 37996, USA*

Abstract

The character of plastic deformation in metallic glasses is investigated through instrumented nanoindentation experiments on amorphous $Pd_{40}Ni_{40}P_{20}$ and $Mg_{65}Cu_{25}Gd_{10}$. Using a customized experimental apparatus, nanoindentation experiments have been conducted over four decades of indentation strain rate and from ambient temperature up to the glass transition, allowing rapid evaluation of an extensive deformation map with only small volumes of experimental material. At low rates and temperatures, inhomogeneous or serrated flow is observed, owing to the discrete operation of individual shear bands. Two distinct regimes of homogeneous flow can be identified. The first, expected, regime of homogeneous flow corresponds to the onset of viscous deformation at high temperatures and low rates, and is well described by existing mechanistic models. The second homogeneous regime occurs at high deformation rates even well below the glass transition, and arises when deformation rates exceed the characteristic rate for shear band nucleation, kinetically forcing strain distribution. By extending an existing model for glass deformation to explore shear band nucleation kinetics, this second regime is quantitatively rationalized and the natural frequency for shear band nucleation is extracted from the data. From this analysis the critical radius of a shear band as it transitions from nucleation to propagation is estimated to be in the submicron range.
© 2004 Acta Materialia Inc. Published by Elsevier Ltd. All rights reserved.

Keywords: Metallic glass; Nanoindentation; Shear bands; High temperature deformation

1. Introduction

Nanoindentation experiments have recently provided some key insights into the mechanisms and mechanics of metallic glass deformation [1]. For example, the nanoindentation load–displacement (*P–h*) curves of various metallic glasses have helped elucidate the asymmetric yield criterion of these materials [1–4], and careful

TEM studies of indented metallic glasses have revealed the presence of ordered or nanocrystalline regions that resulted from local mechanical deformation [1,5,6]. A growing number of authors have considered the formation of individual shear bands by nanoindentation [1,2,7–14], where displacement bursts in the *P–h* response have been correlated with discrete shear banding events.

In recent work, Schuh et al. [2,8–10] identified a rate dependency to the nanoindentation response of metallic glasses, wherein slow indentations exhibited serrated *P–h* curves with many distinct displacement bursts, while more rapid indentation rates could partially or even

completely suppress the appearance of such bursts. This result is nominally counterintuitive, as metallic glasses are well known to exhibit homogeneous flow at low strain rates, while shear instabilities (and serrated flow) usually dominate at high rates [15,16]. Because of this apparent inconsistency, several authors have suggested that the rate-dependence observed in nanoindentation experiments was possibly due to instrumental artifacts [7,11]. In contrast, Schuh et al. [2] have proposed that these results in fact demonstrate a true material response, and constitute a new high-rate regime of homogeneous flow on the deformation map of metallic glasses. They proposed that the counterintuitive nature of the results arises because of the dominance of shear band *nucleation kinetics* at high deformation rates. Specifically, those authors suggested that in nanoindentation experiments the nucleation of an incipient shear band beneath the indenter tip can be rate limiting to the deformation, such that rapid indentations can exceed the natural frequency of shear band nucleation. Based on this reasoning, Schuh et al. [2] identified a critical indenter velocity of the order $\sim 1 \ \mu m \, s^{-1}$ at low temperature, below which individual shear bands would discretely accommodate the deformation, and above which many shear bands would likely coexist and serrated flow would cease. In practice this transition is not abrupt at the critical velocity, but occurs gradually over several orders of magnitude in indentation strain rate.

In addition to explaining the smoothing of experimental *P–h* curves for metallic glasses indented at high rates, the nucleation-limited view of shear banding in metallic glasses gives rise to several natural predictions that can be unambiguously experimentally validated:

(1) This model predicts that rapid indentations would produce more shear bands of a smaller size; e.g., the amount of strain localized into one large shear band at low rates would instead be dispersed among many shear bands of smaller shear displacement at high rates. This expectation has been strikingly validated by the experimental results of Jiang and Atzmon [7] on an aluminum-based metallic glass, where slow indentations were shown to produce serrated *P–h* curves as well as large, widely spaced shear bands on the specimen surface, while more rapid indentations exhibited homogeneous flow and a high number density of smaller shear bands.

(2) Because nucleation kinetics depend on homologous temperature as well as glass structure and chemical order, etc., the nucleation-limited model predicts that different metallic glasses should exhibit tangibly different kinetics. In particular, the critical strain rate separating homogeneous from serrated flow would be expected to vary from one glass to another. Since the early observation of this effect in Pd–Ni–P glass [8], additional experimental studies on two Zr-based [9], one La-based [10], and one Al-based metallic glass [7] have validated this

prediction. As summarized in [1], these various glasses exhibit critical strain rates or indentation velocities that vary by over an order of magnitude.

(3) The nucleation-limited model of serrated flow predicts that, as would be the case for any nucleation process, elevated temperatures should promote shear bands by lowering the activation barrier for their formation. Accordingly, modest elevation of the indentation temperature should give rise to more serrated flow.

The purpose of this paper is to explore the proposed transition from discrete to homogeneous plastic flow of metallic glasses at high deformation rates. Experimentally, we perform an exhaustive set of nanoindentation experiments at both ambient and elevated temperatures. In addition to validating prediction (3) above for the first time, we also construct a deformation map that delineates a temperature-dependent regime at high strain rates where glass plasticity becomes more homogeneous. Theoretically, we extend a classic mechanistic model of glass plasticity to validate the experimental observations, and to identify two unique domains of homogeneous flow in the deformation map of metallic glasses.

2. Experimental

The metallic glasses used in the present study were $Pd_{40}Ni_{40}P_{20}$ and $Mg_{65}Cu_{25}Gd_{10}$, provided in the form of rods several millimeters in diameter; details of these particular alloys are available in [17–19]. Each material was metallographically sectioned and polished to a mirror finish prior to mounting for nanoindentation experiments.

Instrumented nanoindentation experiments were performed using a Triboindenter (from Hysitron, Inc., Minneapolis, MN), which has several unique features critical to the present study. First, discrete flow events are well-resolved in the Triboindenter, due to rapid instrument response and data acquisition rates on the order of $10^4 \, s^{-1}$. Second, this instrument allows indentation loading rates up to about $10^3 \, mN \, s^{-1}$, and can access over four orders of magnitude in indentation strain rate. Finally, a commercial heating stage mounted in the Triboindenter allows heating of the specimen to about 75 °C, and with some modification we have been able to achieve much higher temperatures ($\sim$275 °C) without loss of resolution [20]. A schematic of the heating stage setup used in this work is illustrated in Fig. 1. The specimen is heated conductively from below, and the displacement transducer is shielded from the hot specimen and stage with a cooled copper fixture. The indenter tip is a Berkovich geometry diamond, mounted to a low thermal conductivity shaft fed through a hole in the cooled heat shield. Temperature is monitored and controlled using a J-type thermocouple in direct contact with the metallic glass specimen, and we have taken care
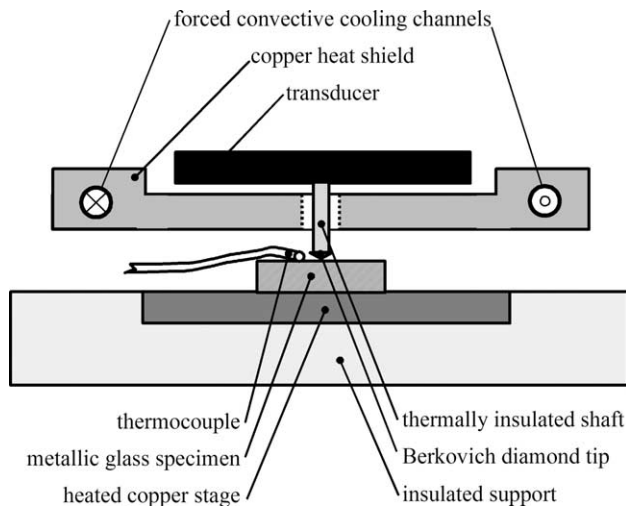
Fig. 1. Schematic of the elevated temperature nanoindentation setup used in the present experiments.

to selectively place indentations within 2 mm of the thermocouple probe tip.

Prior to indentation experiments, the tip was brought into contact with the specimen surface at a very light load of ~2 μN, and the entire system allowed to thermally equilibrate for more than an hour. For all subsequent indentations performed at the same temperature, the tip was maintained in contact with the specimen surface to promote thermal stability, and moved from one location to the next while maintaining the set-point load of 2 μN. Provided that the system was allowed to equilibrate (with the tip in contact) for more than about an hour, we found that thermal drift became essentially negligible and the natural resolution of the instrument could be maintained without significant additional noise, even to 275 °C. Using a separate thermocouple behind the heat shield, we verified that the transducer did not see elevated temperatures even while the sample was maintained within ±0.3 K of the setpoint.

The indentations in this work were all performed with a maximum load of 9.0 mN, applied in open-loop (load-control) mode with a constant loading rate that ranged from 3×10^{-2} to 300 mN s^{-1}. Indentations were performed at room temperature and at several elevated temperatures; for $Pd_{40}Ni_{40}P_{20}$ the maximum temperature investigated was 200 °C, below the glass transition of $T_g \approx 303$ °C [21], while in $Mg_{65}Cu_{25}Gd_{10}$ the maximum test temperature was 150 °C, slightly above $T_g \approx 135$ °C [19]. The data presented here were acquired during a single continuous heating sequence; each new test temperature was attained by directly heating from the previous one, without intermediate cooling. The effects of annealing and diffusive structural relaxation are not studied here, and will be the domain of future research.

After all of the experiments were complete, the specimens were cooled to room temperature and inspected. In the case of $Pd_{40}Ni_{40}P_{20}$, which was heated to 200 °C, the specimen surface retained a metallic luster. The $Mg_{65}Cu_{25}Gd_{10}$ specimen also retained a metallic luster after heating to 150 °C, but did exhibit slight discoloration after the elevated temperature exposure. As neither specimen exhibited a significant oxide scale, and because the indentations we performed here were generally rather deep (~250 nm), we neglect the possibility of artifacts from thermal oxides in the measured nanoindentation response.

3. Results and analysis

Typical nanoindentation results from the $Pd_{40}Ni_{40}P_{20}$ glass are illustrated in Fig. 2. Since we are interested primarily in the presence or absence of serrated flow in the present work, only the loading portions of the P–h

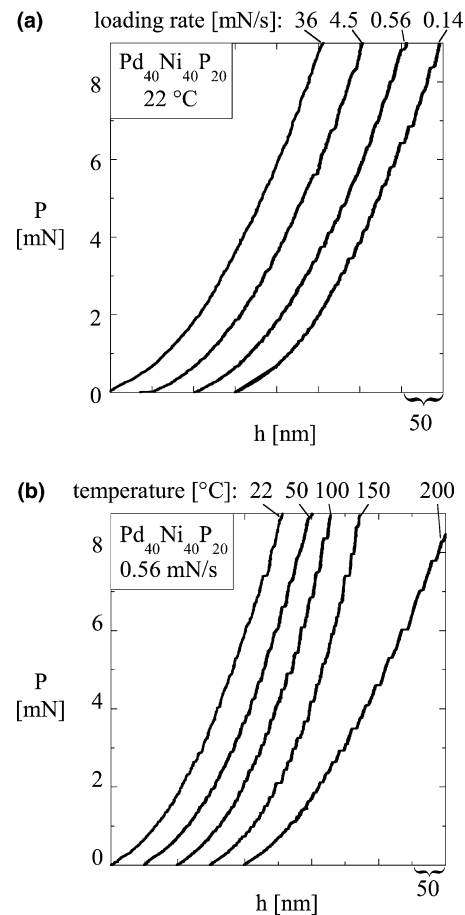Fig. 2. Example load–displacement (P–h) curves obtained by nanoindentation of $Pd_{40}Ni_{40}P_{20}$ metallic glass. Here we show only the loading portion of the curve, and the origin of each curve has been offset to more clearly illustrate: (a) the effect of different loading rates at room temperature and (b) the effect of elevated temperatures at a constant loading rate. Increases in rate or temperature both appear to promote horizontal displacement bursts in these curves.

curves are shown in Fig. 2, and multiple curves have been plotted on the same set of axes with their origins offset for clarity of presentation. In Fig. 2(a), the effect of indentation rate is presented for tests conducted at room temperature. Here we see the same result described in prior research on various metallic glasses [1,2,7–9], namely, that slower deformation rates promote the emergence of serrated flow, in which the P–h curve becomes punctuated by short horizontal 'pop-in' events. The trend seen in Fig. 2(a) has in fact been observed in the same Pd-based glass in [9], although the curves in that work exhibit a somewhat different shape due to the different tip geometry used in that study (roughly spherical in that work compared with pyramidal Berkovich here). We also observe that the shape of the P–h curve is roughly invariant with loading rate, which agrees with the common result that the strength (hardness) of metallic glass is essentially rate-independent at ambient temperature [15,17,18,22–24].

In Fig. 2(b) the effect of temperature on the nanoindentation response of $Pd_{40}Ni_{40}P_{20}$ is shown, for several indentations performed at the same loading rate of 0.56 $mN s^{-1}$. There are two important observations to be made from the data in Fig. 2(b). First, we observe that the maximum depth of the indentations does not change very much as temperature is increased to 150 °C, but then at 200 °C there is a rather sudden increase in the indentation depth. This trend suggests that the glass retains about the same hardness up to about $T/T_g \approx 0.75$, beyond which it suddenly weakens; this trend is in fact general to metallic glasses and has been discussed at length elsewhere [16,24–28]. Second, we observe that as the temperature increases, there is a clear accentuation of serrated flow; the prominence of pop-in events increases significantly with temperature to 200 °C. Although we know of no prior reports of this trend under indentation loading, early data for Pd–Cu–Si glasses revealed a similar effect under compression [28], notch bending [29] and shear tearing [30] modes of loading.

Typical P–h curves for the $Mg_{65}Cu_{25}Gd_{10}$ glass are shown in Fig. 3. In Fig. 3(a) we again see the trend towards increasingly discrete flow with slower indentation rates; to our knowledge this is the first such report for a Mg-based metallic glass. Fig. 3(b) shows the role of temperature in the P–h response of the Mg-glass, and exhibits distinctly different behavior from the Pd-based glass in Fig. 2(b). We observe first that whereas the Pd-glass did not exhibit significant weakening up to 150 °C, the Mg-glass weakens monotonically with the test temperature over the same range. Second, where temperature encouraged serrated flow in $Pd_{40}Ni_{40}P_{20}$, the density and size of pop-in events in the P–h curve clearly decreases continuously with temperature in $Mg_{65}Cu_{25}Gd_{10}$.

The raw P–h data presented in Figs. 2 and 3 is useful to illustrate similarities and differences among a few iso-
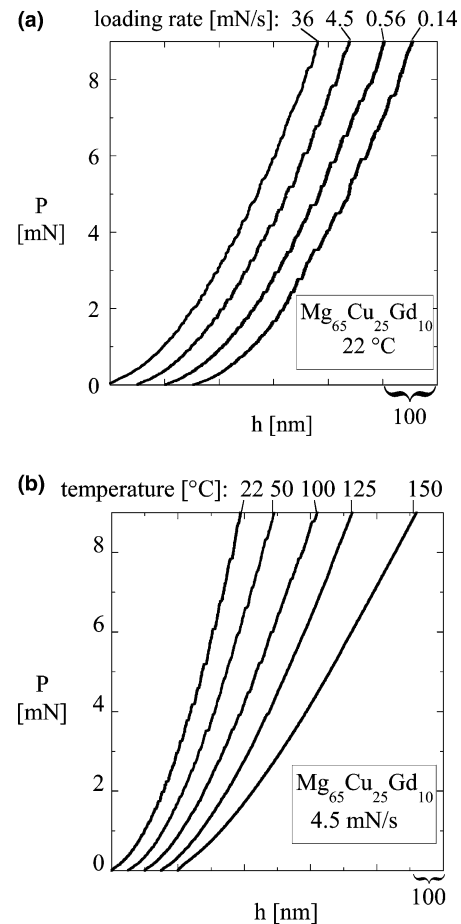

Fig. 3. P–h curves obtained (a) at ambient temperature and different rates and (b) at a constant rate but multiple temperatures, for the $Mg_{65}Cu_{25}Gd_{10}$ glass.

lated tests, but full appreciation of glass deformation dynamics in temperature-rate space requires some reduction of the data. At present, we are interested primarily in the serrated flow behavior of these metallic glasses, so we have analyzed in great detail the pop-in behavior of the nanoindentation data; for this purpose we have used the method of [9]. In this approach the total amount of indentation depth due to pop-in events (serrations) is assessed, and normalized by the residual plastic depth of the indentation. The resulting non-dimensional quantity, $h_{discrete}/h_{plastic}$, gives the fraction of plastic deformation that can be attributed to discrete pop-in events for a given indentation; this parameter is an index of flow serration, being equal to zero for perfectly homogeneous flow and unity for perfectly discretized deformation.

In the present work we have assessed $h_{discrete}/h_{plastic}$ by first calculating the instantaneous indenter velocity, and employing a numerical filter to identify moments during which the indenter was rapidly 'popping-in'. As described in detail in [8,9], spikes in indenter velocity can handily distinguish individual flow serrations, and the value of $h_{discrete}$ is then identified by numerically

integrating the displacement that occurs over all such spikes. The value of $h_{plastic}$ is obtained directly from the residual indentation depth following unloading. We have found that the value of $h_{discrete}/h_{plastic}$ is generally reproducible to within about ±0.05 for indentations performed under identical conditions on the same specimen.

In Fig. 4 the flow serration index $h_{discrete}/h_{plastic}$ is plotted as a function of the indentation rate for the Pd-based (Fig. 4(a)) and Mg-based (Fig. 4(b)) glasses, at several different temperatures. At room temperature, slower indentations give rise to roughly log-linear increases in the discrete contribution to plasticity. In the case of $Pd_{40}Ni_{40}P_{20}$ the room temperature data are numerically quite close to the previously published data using a different indenter tip [9]. In the case of $Mg_{65}Cu_{25}Gd_{10}$ the data exhibit a slight downward concavity at lower loading rates, but it remains generally clear that, at room temperature, low indentation rates promote serrated flow in this alloy as well.

In contrast to the ambient temperature data, the effects of temperature are decidedly unique for the two different glasses in Fig. 4(a) and (b). In the Pd-based glass the entire curve of $h_{discrete}/h_{plastic}$ rises as the temperature is raised from 22 to 150 °C. At 150 °C, the data begin to exhibit some curvature, suggesting that there

may be a turn-over at very low indentation rates. The data at 200 °C are not shown in Fig. 4(a) for the sake of clarity, but these data also exhibited a downward concavity, and in fact the values of $h_{discrete}/h_{plastic}$ decrease slightly from those at 150 °C at virtually all indentation rates. Together, these results suggest that modest temperature increases promote serrated flow in $Pd_{40}Ni_{40}P_{20}$, but high enough temperatures can eventually reverse this trend, especially at low deformation rates.

In the Mg-based glass there is no evidence that temperature increases flow serration at any loading rate. Instead, the vague curvature seen at room temperature becomes increasingly clear as the peak of the data shifts to higher rates with increasing temperature. The consequence of this result is that at any rate, flow gradually homogenizes up to $\sim T_g$, beyond which there is no significant sign of serrated flow at any of the rates studied. As a final note before proceeding, we observe that the data for the Pd-glass at 100 and 150 °C (Fig. 4(a)) are quite similar in form and magnitude to those for the Mg-glass at 22 °C (Fig. 4(b)). In terms of homologous temperatures, all of these data were acquired near $T/T_g \approx 0.7$; this result foreshadows a significant collapse of the data when it is properly scaled for compositional effects.

4. Discussion

The results presented above illustrate that the distinction between serrated and homogeneous flow in metallic glasses is quite complicated. In both $Pd_{40}Ni_{40}P_{20}$ and $Mg_{65}Cu_{25}Gd_{10}$ we observe that higher deformation rates appear to promote homogenization of flow at room temperature, while elevated temperature can either promote or suppress flow serration depending upon the applied indentation rate and the alloy composition. Although at first glance the two different metallic glasses appear to exhibit completely distinct temperature dependencies (Fig. 4), we find that all of the data in this study can be quantitatively collapsed into a generalized physical framework by construction of a properly scaled deformation map.

In the discussion to follow, we first construct an empirical deformation map on the basis of the nanoindentation results, which allows us to clearly separate those behaviors expected on the basis of prior theory, from those which have no mathematical underpinning until now. Subsequently, we draw upon a mechanistic model of glass deformation to justify some of the present results, and then extend this model to the regime of high strain rates to explain others.

4.1. Deformation map

Spaepen [15] was the first person to construct a deformation map for metallic glasses, along the lines of the
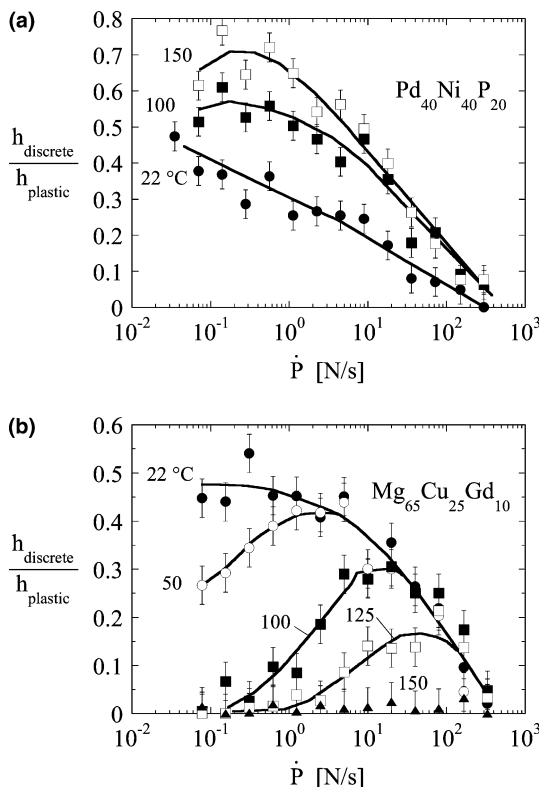

Fig. 4. The ratio of discrete displacement to total plastic displacement for indentations at various loading rates and temperatures, for (a) $Pd_{40}Ni_{40}P_{20}$ and (b) $Mg_{65}Cu_{25}Gd_{10}$. This ratio is essentially an index of how perfectly serrated the plastic deformation is. The solid lines are presented only to highlight trends.

common deformation mechanism maps compiled for crystalline metals [31]. For metallic glasses the term 'deformation mechanism map' is reduced merely to 'deformation map' because it is believed that the mechanism of plastic flow is, for any combination of stress and temperature, the same. In the view of free-volume type models [15,24,32,33] the basic mechanism is a local atomic-scale redistribution of free volume, while in the view of shear transformation zone (STZ) type models [16,34–37] the mechanism is atomic-scale shear distortions (that also influence glass structure and free volume). In either case, it is envisioned that the fundamental unit of plastic flow is the same everywhere on the deformation map, and only the *spatial distribution* of these units (i.e., homogeneous vs. inhomogeneous) is influenced by changes in stress, rate, and/or temperature. In the original work of Spaepen [15] this view led to the division of viscous, homogeneous flow at high temperatures (and/or low stresses) from inhomogeneous shear banding at low temperatures (high stresses). Recent work by Johnson and colleagues [24,32] and others [38] has extended these considerations to delineate regimes of Newtonian and non-Newtonian homogeneous flow in the supercooled liquid regime.

Following [15], we have compiled our nanoindentation data into a deformation map, as illustrated in Fig. 5. For this exercise we have normalized data like those in Fig. 4 in several ways. First, temperature has been scaled by T_g. Second, indentation loading rate has been replaced by an approximate shear strain rate, $\dot{\gamma}_{eff}$. This was accomplished by first examining the indentation strain rate ($\dot{\varepsilon}_i = h^{-1} \cdot dh/dt$) of each experiment, as done in [9], and identifying a reasonable average value; although $\dot{\varepsilon}_i$ actually varies as $1/h$ during a given test, it does level off to within about a factor of two after about the first 50 nm of travel. The effective shear strain

rate is then related to the indentation strain rate by a constant ($\dot{\gamma}_{eff} \approx 0.16 \cdot \dot{\varepsilon}_i$) that incorporates (i) an approximate conversion from indentation to uniaxial strain rate [9,39], and (ii) the usual $\sqrt{3}$ proportionality between uniaxial and shear strain rate. Finally, the flow serration index, $h_{discrete}/h_{plastic}$, has been binned into three categories corresponding to heavily serrated, moderately serrated, and lightly serrated (or homogeneous) flow. This binning procedure was accomplished by simply dividing the full measured range of $h_{discrete}/h_{plastic}$ into thirds, and is used merely as a convenience for clarity of presentation in Fig. 5; other binning procedures give essentially identical results to those presented here.

Before proceeding to a physical discussion of the deformation map, we note that the data from the two different glass compositions superpose quite well in Fig. 5 with the temperature axis normalized by T_g. It seems likely that an even better agreement could be obtained if the strain rate axis were properly scaled by an intrinsic characteristic frequency (e.g., the Debye frequency). Since we are not aware of experimental measurements of the Debye frequency in $Mg_{65}Cu_{25}Gd_{10}$ we have not performed this normalization here, but the shift of the data in Fig. 5 is expected to be no more than about a factor of two; future work will incorporate these kinds of subtle corrections, which do not substantively impact the discussion to follow.

The deformation map presented in Fig. 5 covers homologous temperatures from 0.5 to above the glass transition, and effective shear strain rates from near the quasi-static range to $\sim$10 s^{-1}. Over this range, three distinct regimes of flow character can be observed. Beginning in the lower right-hand corner of the map, we observe that high temperatures near T_g promote homogenous flow. This regime gives way to serrated flow as the temperature is reduced, or as the strain rate
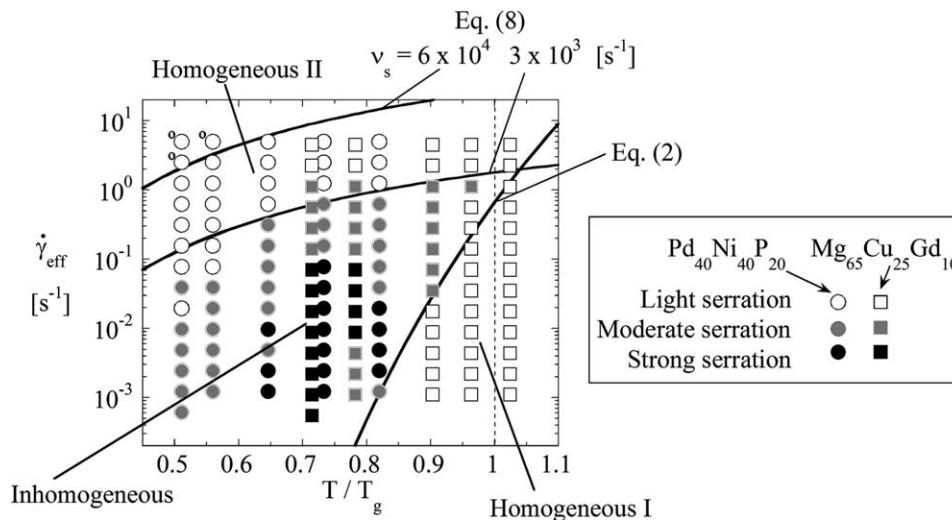

Fig. 5. The deformation map of $Pd_{40}Ni_{40}P_{20}$ and $Mg_{65}Cu_{25}Gd_{10}$ metallic glasses, plotting the effective strain rate during indentation vs. the homologous test temperature. The symbols are shaded according to the degree of flow serration, and the transitions from inhomogeneous to homogeneous flow are described by the mechanistic models developed in the text.

is increased. This behavior is that expected on the basis of prior experiments and theory pertaining to glass deformation, and represents the transition from viscous flow to shear banding delineated in the original deformation map of Spaepen [15]. We denote these two regimes on the map as "Homogeneous I" and "Inhomogeneous".

The third unique regime of flow character observed in Fig. 5 occurs at high strain rates for all of the investigated temperatures, although its boundary with the "Inhomogeneous" regime is clearly temperature-dependent. In this regime flow serration is significantly reduced or even eliminated, and we label it "Homogeneous II". This regime represents the nominally unexpected homogenization of flow at high deformation rates that has been observed in nanoindentation tests at room temperature (see Section 1), and whose physical plausibility has been debated in the literature. What becomes clear from the new data in Fig. 5 is that this unexpected regime of homogeneous flow ("Homogeneous II") is distinct from the expected viscous flow regime ("Homogeneous I") at low rates and high temperatures. The present data set offers strong support that the "Homogeneous II" regime is physically existent, and not an artifact of instrumentation; the shape of this regime is clearly dependent on T/T_g, while any characteristic behavior of the apparatus would not be.

In the sections to follow we will present and further develop the mechanistic models required to quantitatively rationalize the two transitions observed in Fig. 5, from inhomogeneous to homogeneous flows of varieties I and II. Before proceeding, we point out that instrumented nanoindentation is particularly well suited to the development of deformation maps, because many combinations of system parameters can be sampled from a very small volume of material in a relatively short time; the high density of data in Fig. 5 is made possible primarily because of the successful development of elevated-temperature nanoindentation. In future work we will further develop the deformation map of metallic glasses to include, e.g., contours of hardness, flow mechanisms above T_g, etc. For the present purpose, however, we will focus only upon serrated vs. homogeneous flow, and physical justification for the flow regimes seen empirically in Fig. 5.

4.2. Mechanistic model of glass deformation

For the purpose of explaining trends in the deformation map of Fig. 5, we will make recourse to one of the original mechanistic models of glass deformation, that developed by Argon [16] and later modified and adapted in [34,35,40]. This model depicts glass deformation as a collective effect arising from the operation of many small atomic-scale shear events, in which a few atoms collectively shuffle in a shear mode under the combined action of stress and temperature. The physical basis for such local shear events was provided by early simulations of amorphous systems [41–44], and more recent simulations [36,37,45] have continued to support this picture of glass plasticity. Various other statistical and computational studies have also grown from the original concept of Argon [46–53], and the term "shear transformation zone" has come to be generally used to describe the local shear events that comprise plasticity. A final advantage of Argon's STZ-based mechanistic model for the present purposes is that the phenomenology of this model is essentially identical to that of the free volume model of Spaepen [15], and physical predictions made with either model are largely equivalent.

Given that an individual STZ has a volume Ω_0 which sustains a shear strain γ_0, Argon calculated the (Helmholtz) free energy required to operate the STZ, ΔF_0, in terms of the elastic properties of the glass:

$$\Delta F_0 = \left[\frac{7 - 5v}{30(1 - v)} + \frac{2(1 + v)}{9(1 - v)} \beta^2 + \frac{1}{2\gamma_0} \cdot \frac{\tau_0}{\mu(T)} \right] \cdot \mu(T) \cdot \gamma_0^2 \cdot \Omega_0, \tag{1}$$

where $\mu(T)$ and v are the temperature-dependent shear modulus and Poisson's ratio of the glass, respectively, and τ_0 is the ideal shear strength of the STZ, i.e., the athermal stress required to activate the shear transformation. The parameter β is a numerical constant that describes the volumetric dilatation of the STZ relative to its shear distortion, and is about equal to unity for amorphous metals. For a metallic glass subjected to a shear stress τ, the strain rate resulting from the superposition of many individual STZ operations is then given as

$$\dot{\gamma} = \alpha_0 v_0 \gamma_0 \cdot \exp\left(-\frac{\Delta F_0}{kT} \right) \sinh\left(\frac{\tau \gamma_0 \Omega_0}{kT} \right), \tag{2}$$

in which α_0 is a constant incorporating the fraction of material that is capable of undergoing shear transformation, v_0 is the natural frequency (attempt rate) of the STZs, k is the Boltzmann constant and T is temperature.

Argon [16] originally derived Eq. (2) for high temperature viscous flow, in which STZs are roughly spherical and there is no spatial correlation between them. He proposed that at lower temperatures (where shear banding occurs) the STZ might change character somewhat, transitioning from spherical to disk-shaped, with a somewhat different value for ΔF. If we neglect these subtleties and assume that STZs have roughly the same character at any rate and temperature, then the main difference in Eq. (2) when shear localization occurs will be in the parameter α_0, as pointed out by Spaepen [15] in the context of the free volume model.

With the mechanistic framework of Eqs. (1) and (2) in hand, we can quantitatively discuss the flow regimes in the deformation map of Fig. 5.

4.3. Inhomogeneous to homogeneous I transition

The transition seen in Fig. 5 from the "Inhomogeneous" to "Homogeneous I" regimes has been known and appreciated for decades, as the gradual emergence of viscous flow at high temperatures. In his original construction of the deformation map, Spaepen [15] delineated these two regimes, and used a free-volume based phenomenology to derive the transition between these zones in temperature-stress space. A similar procedure was also carried out using the STZ-based model of Eq. (2) by Megusar et al. [40]. Those authors found that the transition occurred at essentially a constant value of $\tau/\tau_0 \approx 0.6$ for amorphous metals, and showed that Eq. (2) directly gives the shape of the inhomogeneous/homogeneous boundary in temperature-rate space. Quantitative evaluation of the "Inhomogeneous" to "Homogeneous I" transition requires only a set of material and structure-related constants to introduce into Eq. (2). In the rest of this work, we will employ constants collected for $Pd_{40}Ni_{40}P_{20}$ and similar Pd-based alloys in Table 1 from [16,21,34,54,55]. We note, however, that the choice of these parameters does not significantly reduce the generality of the results that follow. Some of the parameters are related to the character of STZs (γ_0, v_0, $\tau_0(\mu)$), and it has been shown that these are essentially general to any amorphous metal [34,55]. Elastic constants certainly vary from one glass to another, but these are small effects in Eq. (2) that are largely accounted for by normalization of T with T_g. Therefore, the results that follow may be reasonably regarded as general for many metallic glasses.

By rearranging Eq. (2) it can be shown that the transition from "Inhomogeneous" to "Homogeneous I" takes the following form on the deformation map:

$$\ln \dot{\gamma} \propto \frac{\mu(T)}{T}. \tag{3}$$

This scaling dictates the shape of the boundary, and is basically unaffected by the choice of parameters in

Table 1. However, although the shape of the curve is fixed, its *position* is not, and in fact varies quite sensitively with the specific numerical values chosen. We have therefore fixed all of the values listed in Table 1, and have chosen the STZ volume Ω_0 as a fitting parameter in this exercise. With this procedure, the transition can be made to match quite closely to the empirical deformation map, as shown in Fig. 5. Emphasizing again that changes in the fitting parameter Ω_0 do not affect the shape of the curve, we observe that the agreement between model and data is excellent. Furthermore, the average size of an STZ we obtain from this procedure, $\Omega_0 = 4.8 \times 10^{-28}$ m^3, is very close to that estimated in the original work of Argon for $Pd_{80}Si_{20}$, 7.7×10^{-28} m^3. The average diameter of an STZ in the present case would be ~ 10 Å, roughly three or four atoms across; this is certainly in good agreement with STZ observations in simulated amorphous systems [36,37,41,42,45].

4.4. Inhomogeneous to homogeneous II transition

While the existing theoretical framework of Eq. (2) can predict the classical transition from shear banding to viscous flow, it says nothing about the transition that we observe from "Inhomogeneous" to "Homogeneous II" at high strain rates. Following on our previous discussion of this transition (see Section 1), we believe that the issue in this case is not related to the dynamics of individual, isolated STZs, but to their collective dynamics during shear band nucleation. We will consider the following, three-stage picture of shear band formation:

(1) A single STZ forms in the matrix, following the transition-state kinetic law underlying Eq. (2).

(2) If the conditions are right, secondary STZs may form in the vicinity of the first. These secondary transitions are assisted by virtue of the first STZ operation, due to two factors. First, a local strain field is produced by the first STZ operation (influencing τ in Eq. (2)), and second, the operation of the first STZ may lead to local free volume creation (influencing τ_0). In a similar fashion, the operation of secondary STZs biases the transformation of tertiary STZs, and so on. A local collection of multiple STZs can be thought of as a 'shear band nucleus' or 'embryonic shear band'.

(3) The transition of a nucleus into a *bonafide* shear band occurs through autocatalytic directed growth, which is characterized by the partitioning of strain rate from the bulk into the shear band. During this stage the strain rate in the shear band nucleus diverges towards infinity; once its maximum velocity is attained nucleation is complete, and the shear band is considered propagating.

Eq. (2), being based essentially on the dynamics of individual STZs, is already an appropriate framework describing Stage 1. As we will see later, Argon has also

Table 1
Collected materials constants used in the mechanistic models of glass deformation

Parameter	Value	Reference
$\alpha_0 \gamma_0 v_0$	10^{11} s^{-1}	[16,55]
γ_0	0.125	[34,55]
μ_0	36.6 GPa [a]	[21]
$d\mu/dT$	2.6×10^{-4} K^{-1} [a]	[54]
v	0.405	[21]
τ_{is}	$0.03 \cdot \mu(T)$	[16]
ε_v	0.5	[16]
$\kappa \varepsilon_v^2$	0.2	[16]
λ	4.56	[16]
D	5	[16]

[a] Shear modulus is a function of temperature given by $\mu(T) = \mu_0(1 - \mu_0^{-1}(d\mu/dT) \cdot (T - 300))$, where μ_0 is the modulus at 300 K.

already provided a mechanical analysis of strain rate partitioning that describes Stage 3. What is missing, however, is a quantitative connection between these models, i.e., a model of Stage 2. In what follows, we consider Stage 2, and model the transition from an isolated STZ to a cluster of STZs that constitutes a shear band nucleus. Connecting these new developments with the existing analysis of Stage 3, we will rationalize the "Inhomogeneous" to "Homogeneous II" transition seen in Fig. 5.

4.4.1. Stage 2: formation of STZ clusters

We begin by dividing the material into two volumes; that very near an STZ which has just transformed and which will become the nucleus of a shear band, and the remainder of the glassy matrix. The matrix volume feels the applied far-field stress, τ, and accordingly flows at a rate given by Eq. (2). The smaller embryonic shear band volume is close to an STZ which has just undergone shear distortion, and which resulted in the local storage of elastic energy of magnitude ΔF_0 and some amount of free volume. Both the stored elastic energy and free volume are expected to aid the shear transformation of neighboring material elements. In order to get an estimate of this effect, we consider just the elastic effect and neglect for the moment the evolution of free volume around the first STZ. The elastic energy of the first shear transformation is stored partly in the volume of the first STZ, and partly in the surrounding material. The neighboring volume then feels an excess bias beyond that of the far-field stress alone, and is accordingly more likely to transform than volume elements far removed in the matrix. If we assume that, on average, the strain energy produced by an STZ is shared equally among the original STZ volume and ~ 12 equal volumes arranged around it in a close-packed configuration, we can write an approximate equation for the average strain rate in the incipient shear band embryo, $\dot{\gamma}_n$:

$$\dot{\gamma}_n = \alpha_0 v_0 \gamma_0 \cdot \exp\left(-\frac{\Delta F_0}{kT}\right) \sinh\left(\frac{\tau \gamma_0 \Omega_0 + \varphi \cdot \Delta F_0}{kT}\right), \quad (4)$$

where φ is the fraction of the transformation strain energy stored in each STZ-sized volume, and is of the order ~ 0.08.

Combining Eqs. (2) and (4), and considering that the stresses associated with shear banding are generally large, we arrive at:

$$\dot{\Gamma}_0 = \frac{\dot{\gamma}_n}{\dot{\gamma}} = \exp\left(\frac{\varphi \cdot \Delta F_0}{kT}\right), \quad (5)$$

where $\dot{\Gamma}_0$ is the ratio of the strain rate in the shear band nucleus to that of the surrounding matrix. Eq. (5) indicates that shear band nucleation begins with a very local region of the glass deforming more quickly than the rest. Further progress of this nucleation event occurs due to

mechanical instability, and is the domain of Stage 3, which will be discussed in the next section.

In Fig. 6, Eq. (5) is plotted as a function of temperature using the constants for $Pd_{40}Ni_{40}P_{20}$ collected in Table 1. We see here a trend that will become important later: as temperature is increased the shear rate in the nucleus decreases relative to that of the surrounding matrix. This result is intuitive, as high temperatures promote rapid viscous flow of the matrix, which we see in Fig. 6 can become nearly of the same order as that in the shear band near the glass transition.

4.4.2. Stage 3: shear band nucleation

For a description of Stage 3 we turn again to the work of Argon [16], who, in addition to deriving the STZ-based phenomenology of Eq. (2), also considered the problem of strain or strain-rate partitioning between a glassy matrix and a local 'nucleus' such as we have described above. Argon envisioned that localization of strain was governed by local increase in free volume, owing to the dilatation ε_v accompanying STZ operation. Beginning with a rule-of-mixtures describing the strain rate in the nucleus, $\dot{\gamma}_n$, relative to that applied globally, $\dot{\gamma}$, he derived a bifurcation equation that describes the dynamics of strain rate partitioning. In the case where the shear band nucleus is negligibly small compared to the bulk, this equation reads:

$$\frac{d\dot{\Gamma}}{d\gamma} = \dot{\Gamma} \cdot \left(\dot{\Gamma} - 1 - \frac{B}{1-2B} \cdot \frac{\dot{\Gamma} \cdot \ln \dot{\Gamma}}{2\kappa \varepsilon_v^2 \cdot \ln(\alpha_0 v_0 \gamma_0/\dot{\gamma})}\right) \cdot \frac{2\kappa \varepsilon_v^2 nD}{1+\kappa \varepsilon_v^2}, \quad (6)$$

with

$$B = \left[\frac{kT}{\lambda \tau_0 \Omega_0} \cdot \frac{\tau_0}{\tau} \cdot \ln \dot{\Gamma}\right]^{\frac{1}{2}}. \quad (7)$$
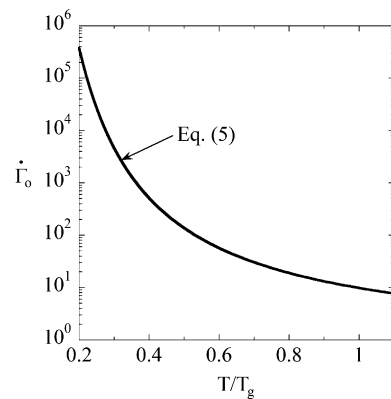

Fig. 6. The ratio of shear strain rate in a forming shear band nucleus (in Stage 2) to that in the surrounding matrix $(\dot{\Gamma}_0 = \dot{\gamma}_n/\dot{\gamma})$, as a function of homologous temperature. As temperature increases the matrix strains more quickly, reducing the value of $\dot{\Gamma}_0$ according to Eq. (5).

In these equations $\dot{\Gamma}$ is the ratio of the local strain rate in the shear band nucleus and the global applied strain rate $(\dot{\gamma}_{n}/\dot{\gamma})$, which evolves from an initial condition $(\dot{\Gamma}_0)$ as strain γ is applied to the material. The terms κ, λ, and D are dimensionless constants, with values assigned as in Table 1 from [16]. The stress sensitivity, $n = \partial \ln \dot{\gamma}/\partial \tau$, can actually be calculated from an appropriate constitutive law such as Eq. (2), and is very high, ≈ 145, for a shear-banding metallic glass [15,16].

When it is numerically integrated, Eq. (6) describes how the strain rate in the shear band nucleus accelerates as shear strain γ is applied to the material; this is illustrated in Fig. 7. At the point where a legitimate shear band has formed and is carrying all of the deformation, $\dot{\Gamma}$ diverges to infinity. This occurs at an applied strain γ_n, which marks the end of the shear band nucleation process, and which depends upon the inputs to Eq. (6). This model captures an important kinetic effect of shear banding; the rate-limiting kinetics occur in the early (nucleation) stages; once γ_n is reached the shear band is propagating at a very high velocity.

In the present context, we are interested primarily in how temperature influences the solution of Eq. (6). Examining the formula, we find that the only temperature dependence is contained in the parameter B of Eq. (7). The parabolic form of Eq. (7), combined with the fact that B appears in both the numerator and denominator in Eq. (6), make the intrinsic temperature dependence of Eq. (6) very small indeed. In fact, for a constant initial condition, the solutions to Eq. (6) at temperatures from $T = 0^+$ to T_g are hardly distinguishable. In light of this, we believe that the most important effect of temperature in the formation of shear bands lies

in the earliest stages of nucleation (Stage 2), where the first few STZs are locally clustering. In this stage the initial condition to Eq. (6) is set by Eq. (5), and this condition, $\dot{\Gamma}_0$, is significantly temperature-dependent, as we saw in Fig. 6. It is primarily due to the different values of $\dot{\Gamma}_0$ that the curves in Fig. 7 are different from one temperature to the next.

The net result of this model is shown in Fig. 8, where the strain required to nucleate a shear band, γ_s, is shown as a function of T/T_g. The curve in this plot was obtained by compiling many individual numerical solutions of Eq. (6) like those shown in Fig. 7. As Fig. 8 demonstrates, these calculations predict that higher temperatures increase the amount of strain required to nucleate a shear band. The reason for this is that shear band nucleation is essentially controlled by the strain rate mismatch between the nucleus and the matrix, and temperature rapidly reduces this mismatch by accelerating viscous flow of the matrix (Fig. 5).

4.4.3. Shear band dynamics

Having quantitative descriptions of each stage of the shear band nucleation mechanism, we can now discuss glass deformation in terms of the *shear band nucleation dynamics*, rather than just on the basis of STZ dynamics. We first observe that qualitatively, the results of the preceding theoretical analysis anticipate the main unexpected finding of our nanoindentation experiments. Fig. 8 illustrates that the strain required to nucleate a shear band increases with temperature, and since shear banding leads to the partitioning of strain primarily into the shear band itself, Fig. 8 also suggests that the shear strain carried by each individual shear band rises with temperature. As long as T is well below the range where general viscous flow occurs, this result suggests that higher test temperatures will promote large shear bands, more widely spaced in time (strain); elevated temperatures promote serrated flow. This result is exactly what
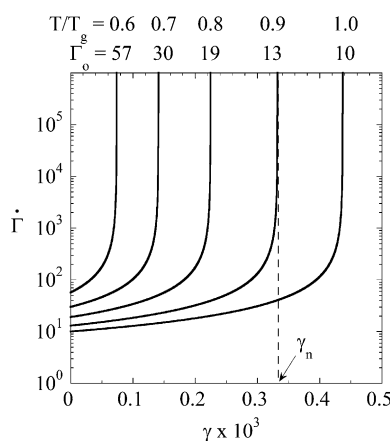
Fig. 7. The evolution of strain rate partitioning as a shear band nucleates, obtained by numerical integration of Eq. (6). As strain γ is applied to the material the ratio $\dot{\Gamma}$ describes the relative strain rate in the shear band embryo as compared to the bulk. Due to the creation of free volume around the growing nucleus, a runaway acceleration occurs, and the shear band is fully formed at a strain γ_n. As the multiple curves illustrate, this process is affected by temperature, mostly through changes in the initial condition.
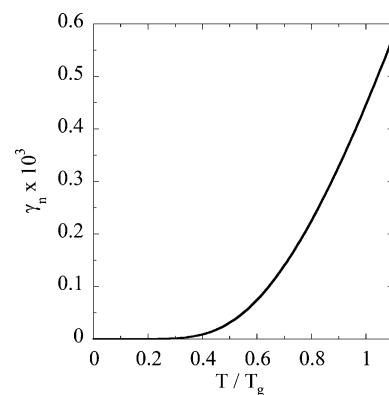
Fig. 8. The shear strain required to fully nucleate a shear band, as a function of homologous temperature. This curve is determined from the numerical solutions to Eq. (6) such as those presented in Fig. 7.

we observe below 150 °C in $Pd_{40}Ni_{40}P_{20}$, qualitatively in Fig. 2(a), and quantitatively in Figs. 4(a) and 5.

If the total constitutive response of the glass is governed by the activation of shear band nuclei, then we can postulate that a similar phenomenology to Eq. (2) would apply to deformation of metallic glasses in the inhomogeneous flow regime, but with STZ dynamics replaced by those of shear band nuclei. By analogy with Eq. (2) we have

$$\dot{\gamma} = \alpha_s v_s \gamma_s \cdot \exp\left(-\frac{\Delta F_s - \tau \gamma_s \Omega_s}{kT}\right), \tag{8}$$

where the subscripts '0' pertaining to STZ characteristics have been replaced with 's' to denote shear band nucleus properties. We expect that whereas there may be a significant 'back-flux' when deformation is controlled by STZ operations, this is relatively unlikely for the (presumably) much larger shear band nuclei, so the hyperbolic sine from Eq. (2) has been replaced with an exponential.

Although we do not know the appropriate form for the exponential arguments in Eq. (8), we can still explore the transition from "Inhomogeneous" to "Homogeneous II" flow, which occurs when the entire volume of material is flowing as if in shear bands, i.e., $\alpha_s \rightarrow 1$. Noting that the strain accommodated by each shear band is $\approx \gamma_n / \alpha_s$, we observe that the transition will require high stresses. In the limit of the highest possible strain rates, $\Delta F_s \approx \tau \Omega_s \gamma_n$, and we can see that the deformation is limited by the athermal 'attack frequency' for shear banding, v_s:

$$\dot{\gamma} \approx v_s \gamma_n. \tag{9}$$

The temperature dependence of Eq. (9) is quite different from that seen in Eq. (3), and resides in the temperature-dependent shear band nucleation strain, γ_n, plotted in Fig. 8. We therefore expect that the shape of the boundary from "Inhomogeneous" to "Homogeneous II" will exhibit a significantly different curvature from that calculated for the typical serrated/viscous flow transition earlier.

Treating v_s as unknown, we proceed by fitting Eq. (9) to the deformation map in Fig. 5. The most appropriate fit to this data set is at the limit where no flow serration can be observed at all. This point occurs when $v_s \approx 6 \times 10^4$ s^{-1}, and is only captured by a few of the experimental data points, which are marked with '0' to denote that no flow serration was detected to within the error of our technique. As shown in Fig. 5, with a somewhat lower value of $v_s = 3 \times 10^3$ s^{-1} Eq. (9) follows the contour between light and moderate serration at the "Inhomogeneous"/"Homogeneous II" border quite reasonably.

The above assessment of v_s is, to our knowledge, the first time that the natural frequency of a shear band nucleus has been inferred from experimental results, and

our final goal is to examine whether its approximate value of 6×10^4 s^{-1} is reasonable. In the present view, the nucleus is regarded essentially as a collection of STZs, each of which has a natural frequency v_0. For a collection of oscillating atoms, either an STZ or a shear band nucleus, we expect that the fundamental vibrational mode of the collection will control its kinetics, and would be inversely proportional to the number of atoms involved in the oscillation [56], N_0 and N_s for STZ and nucleus respectively. We write, then

$$v_s = \frac{N_0}{N_s} v_0 = \frac{N_0}{N_s} \cdot \frac{(\alpha_0 v_0 \gamma_0)}{\alpha_0 \gamma_0}. \tag{10}$$

Here the term in parenthesis is the one tabulated in Table 1, and was determined from high-temperature creep experiments [55]; under these conditions α_0 is of order unity.

Using Eq. (10), we can infer that a shear band nucleus contains about $N_s/N_0 \approx 10^7$ times as many atoms as does a single STZ. From our earlier discussion of the "Inhomogeneous"/"Homogeneous I" transition, we know that each STZ contains about 30 atoms, so the number of atoms involved in the shear band nucleus just as it goes critical and enters a 'propagation' stage is $\sim 10^8$. Taking the incipient shear band to be a disk of typical thickness ~ 10 nm, the nucleus would then have a diameter on the order of 0.5 μm. This size is surprisingly large, but likely reasonable, being much smaller than a typical test specimen; we know of no other direct evidence to corroborate the shear band nucleus size we have found here. It is interesting to note that in nanoindentation experiments, the very first shear bands to form are smaller than the critical size determined here. This implies that for very shallow indentations, the shear band need never accelerate to its full propagation speed before the applied strain is relaxed. This then offers an experimental approach to study individual shear band nuclei before they are fully formed, and presents a direction for future research.

We conclude this discussion with a note of caution in interpreting the present results. Although both "Homogeneous I" and "Homogeneous II" regimes are characterized by the loss of flow serration, the physical origin of these two regimes is clearly quite different. In homogeneous flow of type I, the smoothing of flow curves arises due to the thermally induced dispersion of STZ activity throughout the bulk, and homogenization of flow *in time* is accompanied by commensurate homogenization *in space*. In the case of "Homogeneous II" flow, the loss of flow serration occurs by virtue of kinetic limitations on shear band nucleation. Although the transition to this regime does involve homogenization of deformation *in both time and space*, these transitions are quite likely separated by a wide margin in strain rate. It is relatively easy to deform the glass quickly enough to promote the simultaneous operation of multiple shear bands, thereby losing

serrations in the flow curve. On the other hand, the complete homogenization of flow in space requires that shear bands effectively consume the entire specimen, and would require significantly higher deformation rates. These comments are supported by a variety of experiments on metallic glasses and metallic glass matrix composites at high strain rates, where shear band density increases with strain rate, but shear bands are clearly present nonetheless [7,17,18,29,57]. The most appropriate application of Eq. (9) to experimental data therefore occurs at even higher strain rates than we have studied here, where flow is fully homogeneous not only in time, but in space as well; this would reduce the size of the shear band nucleus estimated above. The issue of adiabatic heating could also significantly influence the transition to spatially homogeneous flow at high rates, although we have not considered such effects here. Finally, we observe that whereas homogeneous flow of type I is typically associated with Newtonian flow and high ductility, type II homogeneous flow is not. The high stress sensitivity ($n > 100$) in the "Homogeneous II" regime will probably persist at higher strain rates, limiting the global ductility of glasses even though they may deform homogeneously.

5. Conclusions

By adapting a commercial nanoindenter to allow testing at up to 200 °C, we have systematically explored the deformation map of metallic glasses $Pd_{40}Ni_{40}P_{20}$ and $Mg_{65}Cu_{25}Gd_{10}$. By focusing on the nature of plastic flow as inhomogeneous (serrated) vs. homogeneous, we have reached the following important conclusions:

- The data from two very different glassy alloys superpose quite well into a single, general deformation map for metallic glasses, provided that the temperature is scaled to the glass transition temperature.
- Inhomogeneous flow, arising from the formation of individual shear bands in a discrete series, is promoted by low temperatures at quasi-static rates. Increasing the temperature at a constant indentation rate sees the gradual emergence of homogeneous flow, as thermal relaxations allow dissipation of strain localization into general viscous flow. This transition is well known in other testing methods, although to our knowledge this is the first exploration of it by instrumented nanoindentation. An existing mechanistic glass deformation model by Argon captures this transition quantitatively, on the basis of STZ dynamics.
- At any of the test temperatures we examined, from 0.5 to $1T_g$, there is a second region of homogeneous flow that occurs at high strain rates, termed the "Homogeneous II" region. While prior nanoindentation experiments have seen this kind of behavior at ambient temperature before, we now see that the transition is temperature-dependent. This regime can be explained on the basis of a kinetic limitation for the nucleation of shear bands. Adapting Argon's model to the treatment of shear band nucleation, we have rationalized the temperature-dependence of this transition.
- Our analysis of the "Homogeneous II" region of the deformation map gives a quantitative estimate for the natural frequency of a shear band nucleus, as well as a critical size for the shear band nucleus just before it reaches the very rapid propagation stage of its lifetime. Assuming a typical thickness of $\sim$10 nm, we expect that shear bands reach a diameter of about a half micron before the applied strain rate fully partitions into the band.

References

[1] Schuh CA, Nieh TG. J Mater Res 2004;19:46.
[2] Schuh CA, Argon AS, Nieh TG, Wadsworth J. Philos Mag A 2003;83:2585.
[3] Vaidyanathan R, Dao M, Ravichandran G, Suresh S. Acta Mater 2001;49:3781.
[4] Patnaik MNM, Narashimhan R, Ramamurty U. Acta Mater 2004;52:3335.
[5] Kim J-J, Choi Y, Suresh S, Argon AS. Science 2002;295:654.
[6] Jiang WH, Pinkerton FE, Atzmon M. J Appl Phys 2003;93:9287.
[7] Jiang WH, Atzmon M. J Mater Res 2003;18:755.
[8] Schuh CA, Nieh TG, Kawamura Y. J Mater Res 2002;17:1651.
[9] Schuh CA, Nieh TG. Acta Mater 2003;51:87.
[10] Nieh TG, Schuh CA, Wadsworth J, Li Y. Intermetallics 2002;10:1177.
[11] Greer AL, Castellero A, Madge SV, Walker IT, Wilde JR. Mater Sci Eng A 2004;375–377:1182.
[12] Greer AL, Walker IT. Mater Sci Forum 2002;386–388:77.
[13] Golovin YI, Ivolgin VI, Khonik VA, Kitagawa K, Tyurin AI. Scripta Mater 2001;45:947.
[14] Wright WJ, Saha R, Nix WD. Mater Trans JIM 2001;42:642.

[15] Spaepen F. Acta Metall 1977;25:407.
[16] Argon AS. Acta Metall 1979;27:47.
[17] Mukai T, Nieh TG, Kawamura Y, Inoue A, Higashi K. Scripta Mater 2002;46:43.
[18] Mukai T, Nieh TG, Kawamura Y, Inoue A, Higashi K. Intermetallics 2002;10:1071.
[19] Men H, Kim DH. J Mater Res 2003;18:1502.
[20] Lund AC, Hodge AM, Schuh CA. Appl Phys Lett 2004;85:1362.
[21] He Y, Schwarz RB, Archuleta JI. Appl Phys Lett 1996;69:1861.
[22] Subhash G, Dowding RJ, Kecskes LJ. Mater Sci Eng A 2002;334:33.
[23] Zhang ZF, Eckert J, Schultz L. J Mater Res 2003;18:456.
[24] Lu J, Ravichandran G, Johnson WL. Acta Mater 2003;51:3429.
[25] Pampillo CA. J Mater Sci 1975;10:1194.
[26] Abrosimova G, Aronin A, Matveev D, Zverkova I, Molokanov V, Pan S, et al. J Mater Sci 2001;36:3933.
[27] Erturk T, Argon AS. J Mater Sci 1987;22:1365.
[28] Pampillo CA, Chen HS. Mater Sci Eng 1974;13:181.
[29] Kimura H, Masumoto T. Acta Metall 1980;28:1663.
[30] Kimura H, Masumoto T. Philos Mag A 1981;44:1021.
[31] Frost HJ, Ashby MF. Deformation-mechanism maps: The plasticity and creep of metals and ceramics. Oxford: Pergamon Press; 1982.
[32] Demetriou MD, Johnson WL. J Appl Phys 2004;95:2857.
[33] Flores KM, Dauskardt RH. Acta Mater 2001;49:2527.
[34] Argon AS, Shi LT. Acta Metall 1983;31:499.
[35] Argon AS. In: Mughrabi H, editor. Material Science and Technology. Weinheim: VCH; 1993. p. 463.
[36] Falk ML. Phys Rev B 1999;60:7062.
[37] Falk ML, Langer JS. Phys Rev E 1998;57:7192.
[38] Nieh TG. Trans Nonferrous Met China 2002;12:726.
[39] Poisl WH, Oliver WC, Fabes BD. J Mater Res 1995;10:2024.
[40] Megusar J, Argon AS, Grant NJ. Mater Sci Eng 1979;38:63.
[41] Argon AS, Kuo HY. Mater Sci Eng 1979;39:101.
[42] Deng D, Argon AS, Yip S. Philos Trans R Soc Lond 1989;329:613.
[43] Argon AS, Shi LT. Philos Mag A 1982;46:275.
[44] Maeda K, Takeuchi S. Phys Stat Sol A 1978;49:685.
[45] Lund AC, Schuh CA. Acta Mater 2003;51:5399.
[46] Bulatov VV, Argon AS. Modell Simulat Mater Sci Eng 1994;2:167.
[47] Bulatov VV, Argon AS. J Non-Cryst Solids 1994;172–174:876.
[48] Bulatov VV, Argon AS. Modell Simulat Mater Sci Eng 1994;2:185.
[49] Bulatov VV, Argon AS. Modell Simulat Mater Sci Eng 1994;2:203.
[50] Eastgate LO, Langer JS, Pechenik L. Phys Rev Lett 2003;90:045506.
[51] Schuh CA, Lund AC. Nat Mater 2003;2:449.
[52] Lemaitre A. Phys Rev Lett 2002;89:195503.
[53] Langer JS, Pechenik L. Phys Rev E 2003;68:061507.
[54] Chen HS. Scripta Mater 1975;9:411.
[55] Argon AS, Kuo HY. J Non-Cryst Solids 1980;37:241.
[56] Nabarro FRN. Theory of crystal dislocations. New York: Dover Publications; 1987.
[57] Kimura H, Masumoto T. Acta Metall 1983;31:231.